In this paper, to achieve macroscopic equilibrium under the given boundary condition and a microscopic self-equilibrium condition efficiently, we propose two new algorithms. First, we show that the algorithm, which is the residual of each scale, decreases simultaneously using block LU factorization without microscopic convergence in the macroscopic iteration as in the conventional algorithm. In addition, an algorithm which approximates the homogenization tangent stiffness using the mode superposition method is proposed. In this method, the same solution as in the original method is preserved with far less computational cost by solving the microscopic equilibrium equation alternately with the solution of the mode superposition-based multi-scale equilibrium equation. Finally, the performance of the proposed method is examined and compared with the conventional method and an example of a simplified multi-scale heart analysis is presented.

2. Nomenclature

$\mathbf{Y}, \mathbf{y}$	:position vector around the deformation in the microstructure
$\mathbf{X}, \mathbf{x}$	:position vector around the deformation in the macrostructure
$\mathbf{u}$	:macroscopic displacement vector
$\{\mathbf{u}\}$	:macroscopic structure nodal displacement vector
$\{\mathbf{u}^e\}$	:macroscopic structure nodal displacement vector per element
$\mathbf{w}$	:periodic component of the microscopic displacement vector
$\{\mathbf{w}\}$	:periodic component of the nodal displacement vectors of all microstructures
$\{\mathbf{w}^Q\}$	:periodic component of the nodal displacement vector of a single microstructure
$\{\mathbf{w}^e\}$	:periodic component of the nodal displacement vector per element
$\mathbf{F}$	:the deformation gradient tensor
$\mathbf{Z}$	:the displacement gradient tensor
$\mathbf{C}$	:the right Cauchy-Green tensor
$\mathbf{E}$	:the Green-Lagrange strain tensor
$\mathbf{\Pi}$	:the first Piola-Kirchhoff stress tensor
$\mathbf{I}$	:the identity tensor
I_c, II_c, III_c	:principal invariants

3. Homogenization Method for Finite Deformation Problem

3.1. Problem Statement and Geometric Prospect

We assume that the material in the body(Ω) reveals heterogeneity on a very fine scale and is characterized by the periodic distribution of a basic structural element(Y_0) as shown in Fig. 1. To measure the changes in the spatial domains, we introduce two scales: a macro-scale $X \in \Omega$ and a micro-scale $Y \in Y_0$. Thus the actual domain can be regarded as the product space ($\Omega \times Y_0$). In the subsequent development, the macroscopic quantity corresponding to the microscopic one is expressed with a bar symbol over the microscopic symbol. The following assumptions of homogenization are employed in the formulation of the homogenization method.

- A macrostructure that consists of a periodic microstructure can be considered to be an approximately equivalent homogeneous substance.
- A microstructure is infinitely fine compared with a macrostructure; the variable defined at each point of the macrostructure corresponds to the volume average of the variables in the microstructure.

The deformation of the microstructure is assumed to be linked to the local values of the macro continuum via

$$\mathbf{y} = \overline{\mathbf{F}}\mathbf{Y} + \mathbf{w}, \tag{1}$$

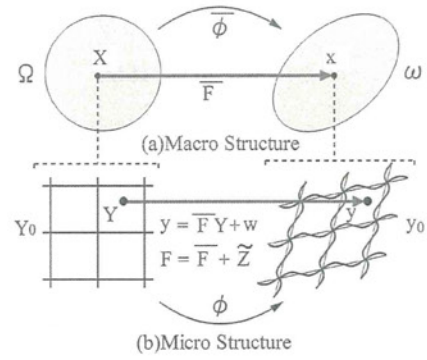

Fig. 1 Homogenization method for large deformation problems

where **y** and **Y** are position vectors defined on the microstructure.

The deformation consists of a homogeneous part $\overline{\mathbf{F}}\mathbf{Y}$ and a non-homogeneous superposed field **w**. Consequently, the following relationships exist between the microscopic and macroscopic deformation gradients.

$$\mathbf{F} = \nabla_Y \mathbf{y} = \frac{\partial \mathbf{y}}{\partial \mathbf{Y}} = \overline{\mathbf{F}} + \tilde{\mathbf{Z}}, \tag{2}$$

$$\overline{\mathbf{F}} = \nabla_X \mathbf{x} = \frac{\partial \mathbf{x}}{\partial \mathbf{X}}, \tag{3}$$

$$\tilde{\mathbf{Z}} = \nabla_Y \mathbf{w} = \frac{\partial \mathbf{w}}{\partial \mathbf{Y}}. \tag{4}$$

Thus increment and variation of the deformation gradients become

$$\Delta\mathbf{F} = \Delta\overline{\mathbf{F}} + \Delta\tilde{\mathbf{Z}} = \Delta\overline{\mathbf{F}} + \nabla_Y \Delta\mathbf{w}, \tag{5}$$

$$\delta\mathbf{F} = \delta\overline{\mathbf{F}} + \delta\tilde{\mathbf{Z}} = \delta\overline{\mathbf{F}} + \nabla_Y \delta\mathbf{w}. \tag{6}$$

For the assumptions mentioned above, the macroscopic gradients are related via the volume averages

$$\overline{\mathbf{F}} = \frac{1}{|V|}\int_{Y_0} \mathbf{F} dY = \frac{1}{|V|}\int_{Y_0} (\overline{\mathbf{F}} + \tilde{\mathbf{Z}}) dY = \overline{\mathbf{F}} + \frac{1}{|V|}\int_{Y_0} \tilde{\mathbf{Z}} dY, \tag{7}$$

where V is the volume of the microstructure Y_0. Then, the fluctuation field **w** has to satisfy the constraint

$$\int_{Y_0} \tilde{\mathbf{Z}} dY = \int_{Y_0} \frac{\partial \mathbf{w}}{\partial \mathbf{Y}} dY = \int_{\partial Y_0} \mathbf{N} \otimes \mathbf{w} dS = \mathbf{0}, \tag{8}$$

where **N** is an outward normal vector on the boundary ∂Y_0. This constraint is satisfied when **w** is periodic.

3.2. Formulation of Homogenization Method and Finite Element Discretization

We consider the equilibrium problem with a periodic microstructure. For the homogenization assumptions, the macroscopic virtual work is related via the volume averages and the entire virtual work represents

$$\int_\Omega \overline{\delta\mathbf{F} : \mathbf{\Pi}} dX = \int_\Omega \frac{1}{|V|}\int_{Y_0} \delta\mathbf{F} : \mathbf{\Pi} dY dX = F_{ext}(\delta u), \tag{9}$$

where $F_{ext}(\delta u)$ is the external virtual work. A similar equation has been reported by Terada et al.[11] using two-scale convergence theory.

By inserting Eq. (6) into Eq. (9), macro and micro equilibrium equations can be derived based on the defined space of the variation.

$$\overline{G} = \int_\Omega \frac{1}{|V|}\int_{Y_0} \delta\overline{\mathbf{F}} : \mathbf{\Pi} dY dX = \int_\Omega \delta\overline{\mathbf{F}} : \overline{\mathbf{\Pi}} dX = F_{ext}(\delta u), \tag{10}$$

$$G = \int_{Y_0} \delta\tilde{\mathbf{Z}} : \mathbf{\Pi} dY = 0, \tag{11}$$

$$\overline{\mathbf{\Pi}} = \frac{1}{|V|} \int_{Y_0} \mathbf{\Pi} dY, \tag{12}$$

which achieves equilibrium under the given boundary condition in the macrostructure and self-equilibrium under the periodic boundary condition Eq. (8) of microscopic displacement in the microstructure. Thus the homogenization method simultaneously satisfies the two equilibrium conditions as described above. To solve the nonlinear equation, the Newton-Raphson method is employed. Then the linearization process provides the following liberalized equations

$$\int_\Omega \frac{1}{|V|} \int_{Y_0} \delta\mathbf{F} : \mathbf{A} : \Delta\mathbf{F} dY dX = F_{ext}(\delta u) - \int_\Omega \frac{1}{|V|} \int_{Y_0} \delta\mathbf{F} : \mathbf{\Pi} dY dX, \tag{13}$$

$$\mathbf{A} = \frac{\partial \mathbf{\Pi}}{\partial \mathbf{F}}. \tag{14}$$

Substituting Eqs. (5) and (6) into the above equation yields

$$\int_\Omega \frac{1}{|V|} \int_{Y_0} (\delta\overline{\mathbf{F}} + \delta\tilde{\mathbf{Z}}) : \mathbf{A} : (\Delta\overline{\mathbf{F}} + \Delta\tilde{\mathbf{Z}}) dY dX =$$

$$F_{ext}(\delta u) - \int_\Omega \frac{1}{|V|} \int_{Y_0} (\delta\overline{\mathbf{F}} + \delta\tilde{\mathbf{Z}}) : \mathbf{\Pi} dY dX. \tag{15}$$

By finite element discretization using

$$\Delta\overline{\mathbf{F}} = [\overline{B^e}]\{\Delta\mathbf{u}^e\}, \tag{16}$$

$$\Delta\tilde{\mathbf{Z}} = [B^e]\{\Delta\mathbf{w}^e\}, \tag{17}$$

the left-hand side of Eq. (15) becomes

$$\{\delta\mathbf{w}^Q\} \frac{1}{|V|} \int_{Y_0} [B^e]^T [A][B^e] dY \{\Delta\mathbf{w}^Q\} + \{\delta\mathbf{w}^Q\} \frac{1}{|V|} \int_{Y_0} [B^e]^T [A] dY [\overline{B^e}]\{\Delta\mathbf{u}^e\} +$$

$$\{\delta\mathbf{u}^e\}[\overline{B^e}]^T \frac{1}{|V|} \int_{Y_0} [A][B^e] dY \{\Delta\mathbf{w}^Q\} + \{\delta\mathbf{u}^e\}[\overline{B^e}]^T \frac{1}{|V|} \int_{Y_0} [A] dY [\overline{B^e}]\{\Delta\mathbf{u}^e\}$$

$$= \{\delta\mathbf{w}^Q\}\mathbf{K}^Q_{ww}\{\Delta\mathbf{w}^Q\} + \{\delta\mathbf{w}^Q\}\mathbf{K}^Q_{wu}\{\Delta\mathbf{u}^e\} + \{\delta\mathbf{u}^e\}\mathbf{K}^Q_{uw}\{\Delta\mathbf{w}^Q\} + \{\delta\mathbf{u}^e\}\mathbf{K}^Q_{uu}\{\Delta\mathbf{u}^e\}, \tag{18}$$

while the second term of the right-hand side of Eq. (15) becomes

$$-\{\delta\mathbf{u}^e\}[\overline{B^e}]^T \frac{1}{|V|} \int_{Y_0} [\Pi] dY - \{\delta\mathbf{w}^Q\} \frac{1}{|V|} \int_{Y_0} [B^e]^T [\Pi] dY, \tag{19}$$

at each quadrature point of the macrostructure. The symbol Q denotes the quantity that is evaluated at the macroscopic quadrature point and symbol e the quantity evaluated in the macroscopic element. By assembling these appropriately on the macro continuum, and considering the facultative variations, the following semi-positive definite symmetric matrix is obtained

$$\begin{bmatrix} \mathbf{K}_{ww} & \mathbf{K}_{wu} \\ \mathbf{K}_{uw} & \mathbf{K}_{uu} \end{bmatrix} \begin{Bmatrix} \Delta\mathbf{w} \\ \Delta\mathbf{u} \end{Bmatrix} = \begin{Bmatrix} \mathbf{r}_w \\ \mathbf{r}_u \end{Bmatrix}, \tag{20}$$

where

$$\mathbf{K}_{ww} = \int_\Omega \left(\frac{1}{|V|} \int_{Y_0} [B^e]^T [A][B^e] dY \right) dX \tag{21}$$

$$\mathbf{K}_{wu} = \int_\Omega \left(\frac{1}{|V|} \int_{Y_0} [B^e]^T [A] dY \right) [\overline{B^e}] dX \tag{22}$$

$$\mathbf{K}_{uw} = \int_\Omega [\overline{B^e}]^T \left(\frac{1}{|V|} \int_{Y_0} [A][B^e] dY \right) dX \tag{23}$$

$$\mathbf{K}_{uu} = \int_\Omega [\overline{B^e}]^T \left(\frac{1}{|V|} \int_{Y_0} [A] dY \right) [\overline{B^e}] dX \tag{24}$$

$$\{\mathbf{r}_w\} = -\int_\Omega \left(\frac{1}{|V|} \int_{Y_0} [B^e]^T [\Pi] dY \right) dX \tag{25}$$

$$\{\mathbf{r}_u\} = \overline{F}_{ext} - \int_\Omega [\overline{B^e}]^T \left(\frac{1}{|V|} \int_{Y_0} [\Pi] dY \right) dX. \tag{26}$$

The nonlinear homogenization method solves Eq. (20) for $\Delta\mathbf{u}$ and $\Delta\mathbf{w}$ under the given boundary condition for the macrostructure and the periodic boundary condition (Eq. (8)) for microscopic displacement. The number of degrees of freedom (NDOF) of this matrix is (NDOF of macrostructure + quadrature point of macrostructure × NDOF of microstructure). An enormous computational cost is also needed for solving the small-scale problem. It is difficult to solve the form given in Eq. (8) due to the limitations of memory, and generally, a transformation into the weak form takes place as described below.

3.3. Characteristic Deformation

In a nonlinear problem, to evaluate the response of a microstructure to macroscopic deformation in a similar way to that in a linear problem[10], we obtain the following equation by taking a derivative of Eq. (11) at each quadrature point and substituting Eqs. (5) and (14).

$$\int_{Y_0} \delta\tilde{\mathbf{Z}} : \mathbf{A} : d\tilde{\mathbf{Z}} dY = -\int_{Y_0} \delta\tilde{\mathbf{Z}} : \mathbf{A} : d\overline{\mathbf{F}} dY. \tag{27}$$

Since the macroscopic deformation gradient is independent of the microscopic integration

$$\int_{Y_0} \delta\tilde{\mathbf{Z}} : \mathbf{A} : \frac{\partial\tilde{\mathbf{Z}}}{\partial\overline{\mathbf{F}}} dY = -\int_{Y_0} \delta\tilde{\mathbf{Z}} : \mathbf{A} : \mathbf{I} dY, \tag{28}$$

where $\mathbf{I}$ is a fourth order identity tensor and the microstructural response of the macroscopic deformation gradient becomes

$$\frac{\partial\tilde{\mathbf{Z}}}{\partial\overline{\mathbf{F}}} = \nabla_Y \left(\frac{\partial\mathbf{w}}{\partial\overline{\mathbf{F}}}\right) \equiv -\nabla_Y \chi, \tag{29}$$

$$\chi \equiv -\frac{\partial\mathbf{w}}{\partial\overline{\mathbf{F}}}, \tag{30}$$

where χ is a third order tensor. This is called the characteristic deformation. The equation above can be substituted into Eq. (28) yielding

$$\int_{Y_0} \delta\tilde{\mathbf{Z}} : \mathbf{A} : \nabla_Y \chi dY = \int_{Y_0} \delta\tilde{\mathbf{Z}} : \mathbf{A} : \mathbf{I} dY. \tag{31}$$

By finite element discretization, the gradient of χ becomes

$$\nabla_Y \chi = [B^e][\chi^e], \tag{32}$$

in a microscopic finite element. $[\chi^e]$ is the derivative of the microscopic displacement for each component of $\overline{\mathbf{F}}$; in other words, it is the matrix given below with nine kinds of characteristic deformation.

$$[\chi^e] = \begin{bmatrix} \chi^e_{111} & \chi^e_{112} & \cdots & \chi^e_{133} \\ \chi^e_{211} & \chi^e_{212} & \cdots & \chi^e_{233} \\ \vdots & \vdots & \ddots & \vdots \\ \chi^e_{n11} & \chi^e_{n12} & \cdots & \chi^e_{n33} \end{bmatrix}, \tag{33}$$

where n is the NDOF of one finite element of the microstructure. The matrix equation becomes

$$\mathbf{K}_\chi[\chi^Q] = [\mathbf{r}_\chi], \tag{34}$$

$$\mathbf{K}_\chi = \int_{Y_0} [B^e]^T [A][B^e] dY, \tag{35}$$

$$[\mathbf{r}_\chi] = \int_{Y_0} [B^e]^T [A][I] dY, \tag{36}$$

from Eq. (31) about one microstructure. $[\chi^Q]$ denotes that the quantity is evaluated at the macroscopic quadrature point. The value of $[\chi^Q]$ which is a (NDOF of the microstructure) row × 9 column matrix can be obtained by assembling $[\chi^e]$. $[I]$ is a ninth order identity matrix, consisting of nine column vectors $\{I_i\}(i = 1 \ldots 9)$. Thus nine solutions can be obtained for the right-hand side of Eq. (36), one for each $\{I_i\}$ corresponding to a component of the deformation gradient. $[\chi^Q]$ can then be obtained by solving each different version of the right-hand side of the above equation.

Multiplying by $[\overline{B^e}]$ and dividing by $|V|$ on both sides, Eq. (34) yields

$$\frac{1}{|V|}\mathbf{K}_\chi[\chi^Q][\overline{B^e}] = \frac{1}{|V|}[\mathbf{r}_\chi][\overline{B^e}]. \tag{37}$$

Now, by using Eq. (18)

$$\frac{1}{|V|}\mathbf{K}_\chi = \mathbf{K}^Q_{ww}, \tag{38}$$

$$\frac{1}{|V|}[\mathbf{r}_\chi][\overline{B^e}] = \mathbf{K}^Q_{wu}, \tag{39}$$

thus

$$\mathbf{K}^Q_{ww}[\chi^Q][\overline{B^e}] = \mathbf{K}^Q_{wu}. \tag{40}$$

The total is taken at all macroscopic quadrature points in respect of the above equation

$$\mathbf{K}_{ww}[\chi][\overline{B}] = \mathbf{K}_{wu}, \tag{41}$$

$$[\overline{B}] \equiv \sum_i [\overline{B^e}], \tag{42}$$

$$[\chi] \equiv \sum_i [\chi^Q], \tag{43}$$

where $[\chi]$ is a matrix consisting of (quadrature points of macrostructure × NDOF of microstructure) rows × 9 columns.

The characteristic deformations are the deformation increments for unit macroscopic deformation gradients at a particular moment and these describe the material properties and strain distribution of the microstructure. Equation (27) can also be considered a linear approximation of the microscopic deformation. Therefore, the update of the microscopic deformation by

$$\Delta\mathbf{w} = -\chi : \Delta\overline{\mathbf{F}}, \tag{44}$$

corresponds to the Forward Euler method for microscopic deformation from Eq. (30).

3.4. Homogenization Method using Characteristic Deformation Mode Superposition

In the mode superposition homogenization method, the microscopic displacement increment is approximately obtained by the linear combination of the previously calculated characteristic deformation ${}_0\chi$ and the scaling factor in Eq. (44) as[6]

$$\Delta w_k \doteqdot -{}_0\chi_{kpQ}\Delta\alpha_{pQ}, \tag{45}$$

where α is the scaling factor for each mode. Inserting Eq. (45) into Eq. (20) yields the matrix

$$\begin{bmatrix} [{}_0\chi]^T & \mathbf{0} \\ \mathbf{0} & \mathbf{I} \end{bmatrix}\begin{bmatrix} \mathbf{K}_{ww} & \mathbf{K}_{wu} \\ \mathbf{K}_{uw} & \mathbf{K}_{uu} \end{bmatrix}\begin{bmatrix} [{}_0\chi] & \mathbf{0} \\ \mathbf{0} & \mathbf{I} \end{bmatrix}\begin{Bmatrix} \Delta\alpha \\ \Delta\mathbf{u} \end{Bmatrix} = \begin{bmatrix} [{}_0\chi]^T & \mathbf{0} \\ \mathbf{0} & \mathbf{I} \end{bmatrix}\begin{Bmatrix} \mathbf{r}_w \\ \mathbf{r}_u \end{Bmatrix} \tag{46}$$

$$\begin{bmatrix} [{}_0\chi]^T\mathbf{K}_{ww}[{}_0\chi] & [{}_0\chi]^T\mathbf{K}_{wu} \\ \mathbf{K}_{uw}[{}_0\chi] & \mathbf{K}_{uu} \end{bmatrix}\begin{Bmatrix} \Delta\alpha \\ \Delta\mathbf{u} \end{Bmatrix} = \begin{Bmatrix} [{}_0\chi]^T\mathbf{r}_w \\ \mathbf{r}_u \end{Bmatrix}. \tag{47}$$

where $[{}_0\chi]$ is the same kind of matrix as $[\chi]$. The above equation can be represented as

$$\begin{bmatrix} \mathbf{K}_{\alpha\alpha} & \mathbf{K}_{\alpha u} \\ \mathbf{K}_{u\alpha} & \mathbf{K}_{uu} \end{bmatrix}\begin{Bmatrix} \Delta\alpha \\ \Delta\mathbf{u} \end{Bmatrix} = \begin{Bmatrix} \mathbf{r}_\alpha \\ \mathbf{r}_u \end{Bmatrix}, \tag{48}$$

where,

$$\mathbf{K}_{\alpha\alpha} = \int_\Omega \left(\frac{1}{|V|}\int_{Y_0} [{}_0\chi^e]^T[B^e]^T[A][B^e][{}_0\chi^e]dY \right) dX \tag{49}$$

$$\mathbf{K}_{\alpha u} = -\int_\Omega \left(\frac{1}{|V|}\int_{Y_0} [{}_0\chi^e]^T[B^e]^T[A]dY \right)[\overline{B^e}]dX \tag{50}$$

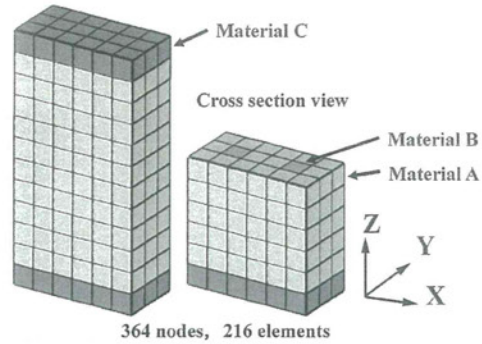

Fig. 2 Simplified cell model

Table. 1 Material constants for simplified cell model

	E [kPa]	ν
Material A in Fig.2	0.1	0.3
Material B in Fig.2	60.0	0.3
Material C in Fig.2	100.0	0.3

$$\mathbf{K}_{u\alpha} = -\int_{\Omega}[\overline{B^e}]^T\left(\frac{1}{|V|}\int_{Y_0}[A][B^e][{}_0\chi^e]dY\right)dX \tag{51}$$

$$\mathbf{K}_{uu} = \int_{\Omega}[\overline{B^e}]^T\left(\frac{1}{|V|}\int_{Y_0}[A]dY\right)[\overline{B^e}]dX \tag{52}$$

$$\{\mathbf{r}_u\} = \overline{F}_{ext} - \int_{\Omega}[\overline{B^e}]^T\left(\frac{1}{|V|}\int_{Y_0}[\Pi]dY\right)dX \tag{53}$$

$$\{\mathbf{r}_\alpha\} = \int_{\Omega}\left(\frac{1}{|V|}\int_{Y_0}[{}_0\chi^e]^T[B^e]^T[\Pi]dY\right)dX. \tag{54}$$

We obtain the matrix with unknowns $\Delta\alpha$ and $\Delta\mathbf{u}$. Because the NDOF of the matrix is reduced to (NDOF of macrostructure + quadrature point of macrostructure × 9), significant computational cost is saved.

This technique is however, an approximate means of achieving equilibrium in a range of displacements representing linear combinations of χ_0, as it is clear from Eq. (54) that χ_0 has an effect on equilibrium. In this way, to approximate the deformation in limited deformation patterns, an approximation error is created depending on the analysis case. This is illustrated using the simplified cell model shown in Fig. 2. For the constitutive equation, the St. Venant hyperelastic material is adopted and the material constants are given in Table 1. The macrostructure consists of one element. The deformation of mode superposition method was compared with the exact method under the same load boundary condition. The initial characteristic deformation used for χ_0 is shown in Fig. 4, while examples of deformation of the microstructure are also shown in Fig. 3. Smooth deformation is achieved for shear deformation in the exact method, while irregular deformation is generated by the mode superposition method.

Such a difference has an effect on the convergence solution of the macroscopic deformation and stress through the framework of homogenization. On the other hand, tensile deformation can be confirmed to be approximately correct. The mode superposition method has low computational cost, but it has an approximation error, although this agrees globally with the exact method.

4. Algorithm for Nonlinear Homogenization Method

4.1. Generalized Algorithm

In Eq. (20), $\{\Delta w\}$ can be statically condensed at the element quadrature point level. $\{\Delta w\}$ becomes

$$\{\Delta\mathbf{w}\} = \mathbf{K}_{ww}^{-1}(\{\mathbf{r}_w\} - \mathbf{K}_{wu}\{\Delta\mathbf{u}\}). \tag{55}$$

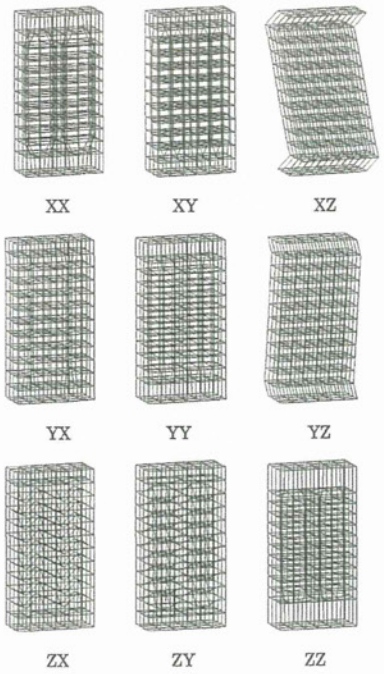

Fig. 3 Characteristic deformations in the initial state

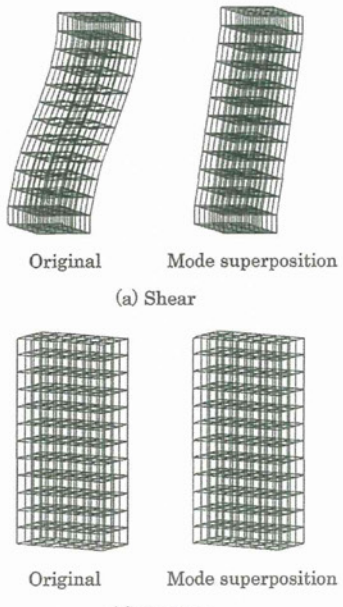

Fig. 4 Disadvantage of characteristic deformation mode superposition

$\{\Delta w\}$ vanishes when the above equation is substituted in the macroscopic equilibrium equation

$$(\mathbf{K}_{uu} - \mathbf{K}_{uw}\mathbf{K}_{ww}^{-1}\mathbf{K}_{wu})\{\Delta\mathbf{u}\} = \{\mathbf{r}_u\} - \mathbf{K}_{uw}\mathbf{K}_{ww}^{-1}\{\mathbf{r}_w\}. \tag{56}$$

Now, the microscopic equilibrium hypothesized for $\overline{\mathbf{F}}$ at this time is

$$\{\mathbf{r}_w\} = 0. \tag{57}$$

By using Eqs. (41) and (55), we obtain[1]

$$\{\Delta\mathbf{w}\} = -\mathbf{K}_{ww}^{-1}\mathbf{K}_{wu}\{\Delta\mathbf{u}\} = -[\chi][\overline{\mathbf{B}}]\{\Delta\mathbf{u}\}. \tag{58}$$

By using Eqs. (41), (55), and (56) we can represent

$$(\mathbf{K}_{uu} - \mathbf{K}_{uw}[\chi][\overline{\mathbf{B}}])\{\Delta\mathbf{u}\} = \{\mathbf{r}_u\}, \tag{59}$$

where $(\mathbf{K}_{uu} - \mathbf{K}_{uw}[\chi][\overline{\mathbf{B}}])$ is called the homogenized tangent stiffness.

In differential equation form, from Eqs. (11), (15), and (29), this becomes

$$\int_\Omega \delta\overline{\mathbf{F}} : \left(\frac{1}{|V|}\int_{Y_0}\left(\mathbf{A} : (\mathbf{I} - \nabla_Y\chi)\right)dY\right) : \Delta\overline{\mathbf{F}}dX$$
$$= \overline{\mathbf{F}}_{ext} - \int_\Omega \delta\overline{\mathbf{F}} : \left(\frac{1}{|V|}\int_{Y_0}\mathbf{\Pi}dY\right)dX. \tag{60}$$

Microscopic equilibrium Eq. (57)

$$r_w = \int_{Y_0}\delta\tilde{\mathbf{Z}} : \mathbf{\Pi}dY = \mathbf{0}, \tag{61}$$

is a prerequisite of the above equation. To satisfy this nonlinear prerequisite, a Newton-Raphson iteration is needed. Thus the above equation is linearized with respect to $\mathbf{w}$ while $\overline{\mathbf{F}}$ is fixed, and then discretized by the finite element method using Eq. (17). At each quadrature point, the linearized self-equilibrated equation becomes

$$\int_{Y_0}[B^e]^T[A][B^e]dY\{\Delta\mathbf{w}^Q\} = -\int_{Y_0}[B^e]^T[\Pi]dY. \tag{62}$$

In the generalized algorithm, three kinds of calculation have to be dealt with in each iteration.

(1) Update macroscopic tangential homogenization χ using Eq. (34).

(2) Solve microscopic equilibrium problem Eq. (61) and obtain the convergence solution $\{\mathbf{w}\}$ while $\overline{\mathbf{F}}$ is fixed.

(3) Solve the linearized macroscopic equilibrium equation Eq. (59) to obtain $\{\mathbf{u}\}$.

Processes 1 and 2 need to be solved at all quadrature points of the macrostructure and it is known that this takes up the greatest part of the calculation load[2]. These processes require prohibitive computational cost and actual numerical simulation is difficult.

4.2. Block LU Factorization Algorithm

We now present the algorithm that decreases the residual of each scale simultaneously using the block LU factorization algorithm without microscopic convergence in the macroscopic iteration as in the conventional algorithm. By Block LU factorization Eq. (20) becomes

$$\begin{bmatrix}\mathbf{K}_{ww} & \mathbf{0}\\ \mathbf{K}_{uw} & \mathbf{S}\end{bmatrix}\begin{bmatrix}\mathbf{I} & \mathbf{K}_{ww}^{-1}\mathbf{K}_{wu}\\ \mathbf{0} & \mathbf{I}\end{bmatrix}\begin{Bmatrix}\Delta\mathbf{w}\\ \Delta\mathbf{u}\end{Bmatrix} = \begin{Bmatrix}\mathbf{r}_w\\ \mathbf{r}_u\end{Bmatrix}, \tag{63}$$

where $\mathbf{S}$ is called the Schur-Complement. Referring to Eq. (41), $\mathbf{S}$ can represent

$$\mathbf{S} = \mathbf{K}_{uu} - \mathbf{K}_{uw}\mathbf{K}_{ww}^{-1}\mathbf{K}_{wu} = \mathbf{K}_{uu} - \mathbf{K}_{uw}[\chi][\overline{\mathbf{B}}]. \tag{64}$$

which corresponds to the homogenized tangent stiffness of Eq. (59). The solution process for Eq. (63) is composed of the forward substitution

$$\begin{bmatrix}\mathbf{K}_{ww} & \mathbf{0}\\ \mathbf{K}_{uw} & \mathbf{S}\end{bmatrix}\begin{Bmatrix}\Delta\tilde{\mathbf{w}}\\ \Delta\tilde{\mathbf{u}}\end{Bmatrix} = \begin{Bmatrix}\mathbf{r}_w\\ \mathbf{r}_u\end{Bmatrix}, \tag{65}$$

and the backward substitution

$$\begin{Bmatrix} \Delta\tilde{\mathbf{w}} \\ \Delta\tilde{\mathbf{u}} \end{Bmatrix} = \begin{bmatrix} \mathbf{I} & \mathbf{K}_{ww}^{-1}\mathbf{K}_{wu} \\ \mathbf{0} & \mathbf{I} \end{bmatrix} \begin{Bmatrix} \Delta\mathbf{w} \\ \Delta\mathbf{u} \end{Bmatrix}. \tag{66}$$

Then, from Eqs. (41), (65), and (66)

$$\mathbf{K}_{ww}\{\Delta\tilde{\mathbf{w}}\} = \{\mathbf{r}_w\}, \tag{67}$$

$$\mathbf{S}\{\Delta\mathbf{u}\} = \{\mathbf{r}_u\} - \mathbf{K}_{uw}\{\Delta\tilde{\mathbf{w}}\}, \tag{68}$$

$$\{\Delta\mathbf{w}\} = \{\Delta\tilde{\mathbf{w}}\} - \mathbf{K}_{ww}^{-1}\mathbf{K}_{wu}\{\Delta\mathbf{u}\} = \{\Delta\tilde{\mathbf{w}}\} - [\chi]\Delta\overline{\mathbf{F}}, \tag{69}$$

hold. The calculation procedure is described below.

(1) Solve linearized microscopic equilibrium equation Eq. (67) to obtain $\{\Delta\mathbf{w}\}$.

(2) Solve linearized microscopic equilibrium equation Eq. (68) to obtain $\{\Delta\mathbf{u}\}$. In addition, this equation is equivalent to Eq. (56).

(3) Update $\{\Delta\mathbf{w}\}$ using Eq. (69). We have already obtained $[\chi]$ when calculating $\mathbf{S}$.

Three kinds of matrix, namely micro, macro, and Schur-Complement, need to be solved in each iteration. The computational cost of this algorithm is lower than the generalized algorithm, but the Schur-Complement update is still expensive as described above. A similar algorithm for a differential equation using the Block-Newton method has been proposed by Yamada et al.[12].

4.3. Mode Superposition as an Approximation of the Macroscopic Tangent Stiffness

In the block LU factorization algorithm, most of the computational cost is consumed by updating the Schur-Complement. But the Schur-Complement is part of the macroscopic tangent stiffness as described above and as such does not influence the equilibrium directly. To avoid updating the Schur-Complement, we propose using Mode superposition as an approximation of the Schur-Complement. The solution agrees completely with the exact method by making a convergence judgment for the microscopic and macroscopic residuals. The calculation procedure is described below.

(1) Solve the linearized microscopic equilibrium equation Eq. (67) to obtain $\{\Delta\tilde{\mathbf{w}}\}$.

(2) From Eq. (48), solve the mode superposition-based linearized multi-scale equation

$$\begin{bmatrix} \mathbf{K}_{\alpha\alpha} & \mathbf{K}_{\alpha u} \\ \mathbf{K}_{u\alpha} & \mathbf{K}_{uu} \end{bmatrix} \begin{Bmatrix} \Delta\alpha \\ \Delta\mathbf{u} \end{Bmatrix} = \begin{Bmatrix} \mathbf{r}_\alpha \\ \mathbf{r}_u \end{Bmatrix}, \tag{70}$$

to obtain $\{\Delta\mathbf{u}\}$. Then, $\mathbf{S}$ is approximated by the range of the mode superposition method and the update of $\mathbf{S}$ can be omitted.

(3) The assumption of the mode superposition method follows from Eqs. (44), (45), and (69), and $\{\Delta\mathbf{w}\}$ is updated using

$$\{\Delta\mathbf{w}\} = \{\Delta\tilde{\mathbf{w}}\} - [_0\chi]\{\Delta\alpha\}. \tag{71}$$

The meaning of the algorithm is now given. Block UL factorization is applied to Eq. (70).

$$\mathbf{K}_{\alpha\alpha}\{\Delta\tilde{\alpha}\} = \{\mathbf{r}_\alpha\}, \tag{72}$$

$$(\mathbf{K}_{uu} - \mathbf{K}_{u\alpha}\mathbf{K}_{\alpha\alpha}^{-1}\mathbf{K}_{\alpha u})\{\Delta\mathbf{u}\} = \{\mathbf{r}_u\} - \mathbf{K}_{u\alpha}\{\Delta\tilde{\alpha}\}, \tag{73}$$

$$\{\Delta\alpha\} = \{\Delta\tilde{\alpha}\} - \mathbf{K}_{\alpha\alpha}^{-1}\mathbf{K}_{\alpha u}\{\Delta\mathbf{u}\}. \tag{74}$$

In Eq. (73), the macroscopic displacement is updated using

$$(\mathbf{K}_{uu} - \mathbf{K}_{u\alpha}\mathbf{K}_{\alpha\alpha}^{-1}\mathbf{K}_{\alpha u}), \tag{75}$$

which can be considered an approximation of the homogenized tangent stiffness. Then, using Eqs. (41) and (64), the Schur-Complement becomes

$$\begin{aligned} &\mathbf{K}_{uw}\mathbf{K}_{ww}^{-1}\mathbf{K}_{wu} = \mathbf{K}_{uw}[\chi]\overline{\mathbf{B}} \\ &= \mathbf{K}_{uw}[\chi]([\chi]^T\mathbf{K}_{ww}[\chi])^{-1}([\chi]^T\mathbf{K}_{ww}[\chi])\overline{\mathbf{B}} \\ &= \mathbf{K}_{uw}[\chi]([\chi]^T\mathbf{K}_{ww}[\chi])^{-1}[\chi]^T\mathbf{K}_{wu} \end{aligned}$$

$$\doteqdot \mathbf{K}_{uw}[\alpha\chi]([\alpha\chi]^T\mathbf{K}_{ww}[\alpha\chi])^{-1}[\alpha\chi]^T\mathbf{K}_{wu}$$
$$= \mathbf{K}_{u\alpha}\mathbf{K}_{\alpha\alpha}^{-1}\mathbf{K}_{\alpha u}. \tag{76}$$

In the mode superposition method, since the homogenized tangent stiffness corresponds to the exact value with the mode updated at every Newton-Raphson iteration as described above, this method can give an approximation mean of the homogenized tangent stiffness by decreasing the number of times that the mode is updated.

In the homogenization method, the micro and macro equilibrium conditions must be achieved simultaneously. To evaluate the residual in each scale, micro and macro equations need to be solved in each iteration and this defines the minimum computational cost. Hence, a requirement for low computational cost in nonlinear homogenization algorithms is to approximate the Schur-Complement effectively and accurately.

5. Numerical Example

5.1. Comparison of Computational Cost and Convergence

We compare computational cost and convergence in the three methods, namely the Generalized algorithm (GA), Block LU factorization algorithm (BFA) and the algorithm using mode superposition (MSA). We did a 20% tensile test using the mesh of the block as the microstructure as shown in Fig. 5, and the mesh of one element of an 8-node element as macrostructure. The minimum size of the mesh is constructed from 27 ($3\times3\times3$) elements as shown in Fig. 5(a) and the stiffness of the center element is different.

The NDOF is adjusted by adding the same number of minimum units in each direction (e.g. Fig. 5(b)). The St. Venant hyperelastic material is used for the constitutive equation

$$W = \frac{1}{2}\lambda(tr\mathbf{E})^2 + \mu\mathbf{E} : \mathbf{E}, \tag{77}$$
$$\mathbf{S} = \frac{\partial W}{\partial \mathbf{E}} = (\lambda\mathbf{I}\otimes\mathbf{I} + 2\mu\mathbf{I}) : \mathbf{E} = \mathbf{C} : \mathbf{E}, \tag{78}$$
$$l_{ijkl} = \delta_{ik}\delta_{jl}, \tag{79}$$
$$\lambda = \frac{E\nu}{(1+\nu)(1-2\nu)}, \quad \mu = G = \frac{E}{2(1+\nu)}, \tag{80}$$

where $\mathbf{I}$ is a second order identity tensor, λ and μ are lame constants, and E and ν are, respectively, Young's modulus and Poisson's ratio. $\mathbf{C}$ is a fourth order constant elasticity tensor and the relationship between $\boldsymbol{S}$ and $\boldsymbol{E}$ is linear. The material constants are shown in Table 2.

The relationship between calculation time and NDOF in each algorithm is depicted in Fig. 6, while the breakdown of calculation time and number of iterations in each process are given in Table 3, where the NDOF is 46875. Convergence is judged to occur when the root sum square is 1×10^{-10} times the initial value. In the BFA, calculation time is reduced only 20% compared with the GA. Because the microscopic and macroscopic problems are solved individually in the GA, the Newton-Raphson methods converged after about 4 iterations. On the other hand, the BFA deals with each system separately and 9 iterations were needed. It can be confirmed that the reason for only a 20% reduction according to Table 3, is as a result of the increase in computational cost due to updating the Schur-Complement. In this analysis, because an iterative solver (GMRES method) is used for the large-scale calculation, it has to solve 9 different right-hand sides to update the Schur-Complement. If a direct method were used, because the result of the LU decomposition of the stiffness matrix can be reused for the different right-hand side solutions and it only solves the equation a single time in practice, the computational cost of the BFA would show a substantially greater decrease than the GA.

We confirmed that the computational cost of the MSA is far less than the other algorithms. The iterations were terminated at the same level as in the BFA but the homogenized tangent stiffness was approximated. Since the microscopic equation is approximately solved in Eqs. (70) and (71) with Eq. (67) by the MSA, the microscopic equation is effectively solved twice. This accelerates convergence. Although we adopted the St. Venant hyperelastic

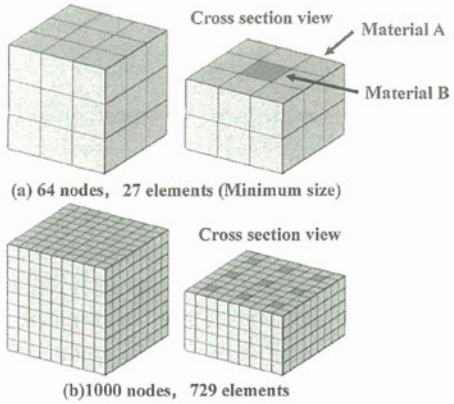

Fig. 5 FE models for the calculation time evaluation

Table. 2 Material constants for the models in the calculation time evaluation

	E[kPa]	ν
Material A in Fig.5	0.1	0.3
Material B in Fig.5	10.0	0.3

material with relatively weak nonlinearity, iterations did not increase in the large deformation although initial characteristic deformation was used for ${}_0\chi$. However, a periodic update of ${}_0\chi$ is required in the case of a strong nonlinear material such as an elasto-plastic material. If ${}_0\chi$ is updated in every iteration, the homogenized tangent stiffness corresponds to the exact value as described in Eq. (76).

5.2. Application to ventricle-cardiomyocyte analysis

We applied the MSA to a simplified left ventricle-cardiomyocyte model as shown in Figs. 7and 8 with the NDOF of the microstructure being 9657. The St. Venant hyperelastic material is adopted for the constitutive equation and the material constants are given in Table 4. The left ventricle model is based on MR imaging, with the ventricle wall divided into three layers, i.e., endocardial, middle and epicardial layers, with fiber directions of -60, 0, and 60 degrees, respectively, relative to the plain perpendicular to the long axis of the LV. The fiber direction in the cardiomyocyte model, shown in Fig. 8, is in the y-direction. The usual St. Venant hyperelastic material is assumed for the base and apex, while a homogenization method is applied to the middle part of 792 elements. Since there are 8 quadrature points at each element, the total number in the cardiomyocyte model is 6336. We use a PC-cluster composed of 99 Pentium 4 (3.2GHz) PCs connected to each other via Myrinet. Considering the size of the problem, convergence is deemed to occur when the root sum square of the macro and micro residuals is 1×10^{-5} times the initial value. The fiber direction is taken into consideration by multiplying the rotational tensor when the micro/macro tensors are exchanged. Since the intracellular matrix is a function of the parameter that represents cardiomyocyte excitation, this

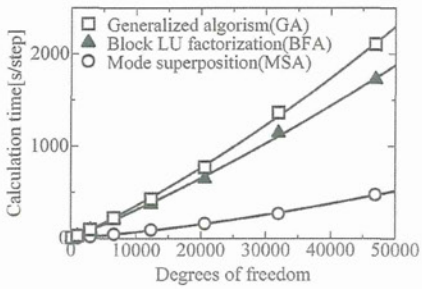

Fig. 6 Comparison of calculation time

Table. 3 Calculation time and number of iterations in each process

	Calculation of χ [s]	Calculation of equilibrium in the microscopic model [s]	Total [s]	Iteration
GA	746	1296	2105	5
BFA	1251	372	1727	9
MSA	16	300	475	8

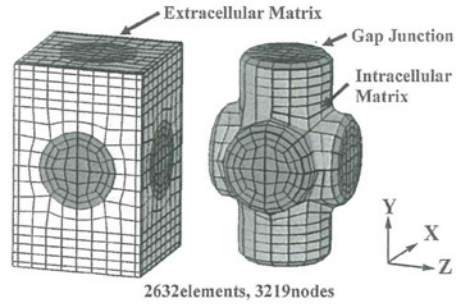

Fig. 7 FE meshes of microscopic model

parameter is adjusted at every time step to represent the contraction force. The deformation of the ventricle and microstructure in the diastole is shown in Fig. 9. The calculation time is 114[s/iteration], 456[s/step] and the number of iterations is about 4 for each step. In this analysis, dilation of the left ventricle by pressure and excitation contraction is generated as a result of the 6336 cardiomyocyte model, which shows the different electrical and mechanical behavior. The proposed methods thus enable us to deal with large scale problems.

Table. 4 Material constants for the cell model

	E[kPa]	ν
Gap Junction	10.0	0.3
Intracellular Matrix	5.0	0.3
Extracellular Matrix	0.1	0.3

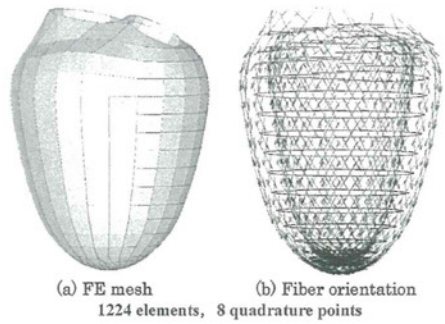

Fig. 8 FE meshes of macroscopic model

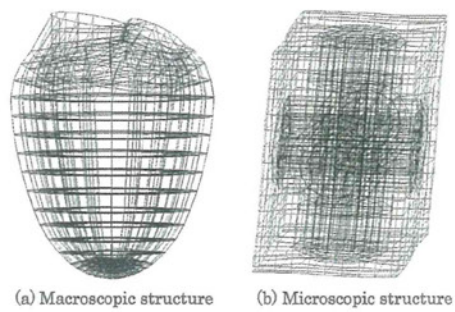

Fig. 9 Deformations in diastole

6. Conclusion

To reduce the computational cost of the nonlinear homogenization method, the two algorithms listed below were proposed.

(1) An algorithm which decreases the residual of each scale simultaneously using the block LU factorization.

(2) An algorithm which approximates the homogenization tangent stiffness using the mode superposition method to omit updating the Schur-Complement.

Both the Block LU factorization algorithm and the algorithm using mode superposition can drastically reduce the computational cost compared with the conventional method. Finally, the algorithm using mode superposition applied to the left ventricle of the heart with parallel computation was presented as an example of a large scale calculation.

Acknowledgment

This work was supported by Core Research for Evolutional Science and Technology, Japan Science and Technology Agency.

References

(1) Terada, K. and Kikuchi, N., A class of general algorithms for multi-scale analyses of heterogeneous media, *Computer Methods in Applied Mechanics and Engineering*, 190, No. 40-41(2001), pp.5427-5464.

(2) Matsui, K., Terada, K. and Yuge, K., Two-scale finite element analysis of heterogeneous solids with periodic microstructures, *Computers & Structures*, 82(2004) pp.593-606.

(3) Takano, N., Ohnishi, Y., Zako, M. and Nishiyabu, K., Microstructure-based Deep-drawing Simulation of Knitted Fabric Reinforced Thermoplastics by Homogenization Theory, *International Journal of Solids and Structures*, 38(2001), pp.6333-6356.

(4) Rohan, E., Sensitivity strategies in modelling heterogeneous media undergoing finite deformation, *Mathematics and Computers in Simulation*, 61(2003), pp.261-270.

(5) Moulinec, H. and Suquet, P., A numerical method for computing the overall response of nonlinear composites with complex microstructure, *Computer Methods in Applied Mechanics and Engineering*, 157(1998), pp.69-94.

(6) Yamamoto, M., Hisada, T. and Noguchi, H., Homogenization Method for Large Deformation Problem by Using Characteristic Deformation Mode Superposition (in Japanese), *Trans. Jpn. Soc. Mech. Eng.*, 67(2001), pp.1877-1884.

(7) Okada, J. and Hisada, T., Homogenization Method for Mixed Finite Element Analysis of Incompressible Hyper-Elastic Materials (in Japanese), *Proceedings of the Conference on Computational Engineering and Science*, 11(2006), pp.79-82.

(8) Okada, J. and Hisada, T., Homogenization Method for Mixed Finite Element Analysis of Incompressible Viscoelastic Materials (in Japanese), *Proceedings of the 19th Computational Mechanics Conference*, No.06-9(2006), pp.45-46.

(9) Miehe, C., Schroder, J. and Schotte, J., Computational Homogenization Analysis in Finite Plasticity. Simulation of Texture Development in Polycrystalline Materials, *Computer Methods in Applied Mechanics and Engineering*, 171(1999), pp.387-418.

(10) Terada, K. and Kikuchi, N., Introduction to the method of homogenization (in Japanese), Maruzen, 2003.

(11) Terada, K., Saiki, I., Matsui, K. and Yamakawa, Y., Two-scale kinematics and linearization for simultaneous two-scale analysis of periodic heterogeneous solids at finite strain, *Computer Methods in Applied Mechanics and Engineering*, 192(2003), pp.3531-3563.

(12) Yamada, T. and Matsui, K., Numerical Procedure for Nonlinear Multiscale Problems Based on Block Newton Method (in Japanese), *Proceedings of the Conference on Computational Engineering and Science*, 12(2007), pp.309-312.

Clinical and Experimental Hypertension, 31:698–704, 2009

ISSN: 1064-1963 print / 1525-6006 online
DOI: 10.3109/10641960903407066

informa
healthcare

Atorvastatin Improves the Impaired Baroreflex Sensitivity via Anti-Oxidant Effect in the Rostral Ventrolateral Medulla of SHRSP

TAKUYA KISHI, YOSHITAKA HIROOKA, SATOMI KONNO, AND KENJI SUNAGAWA

Department of Cardiovascular Medicine, Kyushu University Graduate School of Medical Sciences, Fukuoka, Japan

We have demonstrated that oxidative stress in the rostral ventrolateral medulla (RVLM), a vasomotor center in brainstem, increases sympathetic nerve activity (SNA) and that oral administration of atorvastatin inhibited SNA via anti-oxidant effect in the RVLM of stroke-prone spontaneously hypertensive rats (SHRSPs). The impairment of baroreflex sensitivity (BRS) is known as the predictive factor of mortality in the hypertension and BRS is impaired in SHRSP. The aim of the present study was to determine whether oral administration of atorvastatin improved the impaired BRS via anti-oxidant effect in the RVLM in SHRSP. Atorvastatin (20 mg/kg/day) or vehicle was orally administered for 28 days in SHRSPs. Systolic blood pressure (SBP), heart rate, and 24-h urinary norepinephrine excretion as an indicator of SNA were comparable between atorvastatin- and control-SHRSP. Thiobarbituric acid-reactive substance (TBARS) levels as a marker of oxidative stress was significantly lower in atorvastatin-SHRSP than in control-SHRSP. Baroreflex sensitivity measured by the spontaneous sequence method was significantly higher in atorvastatin-SHRSP than in control-SHRSP. These results suggest that atorvastatin improves the impaired BRS in SHRSP via its anti-oxidant effect in the RVLM of SHRSP.

Keywords statin, oxidative stress, brain, hypertension, baroreflex

Introduction

Rostral ventrolateral medulla (RVLM) in the brainstem is the vasomotor center that determines basal sympathetic nerve activity, and the functional integrity of the RVLM is essential for the maintenance of basal vasomotor tone (1–3). We have demonstrated that oxidative stress in the RVLM increases the sympathetic nerve activity (4), and that nitric oxide (NO) in the RVLM decreases the sympathetic nerve activity (5,6). Previously, we also demonstrated that overexpression of endothelial NO synthase in the RVLM of Stroke-prone

Received August 31, 2008; revised November 11, 2008; accepted November 14, 2008.
Address correspondence to Takuya Kishi, Department of Cardiovascular Medicine, Kyushu University Graduate School of Medical Sciences, 3-1-1 Maidashi, Higashi-Ku, Fukuoka 812-8582, Japan; E-mail: tkishi@cardiol.med.kyushu-u.ac.jp

spontaneously hypertensive rats (SHRSPs) improved the baroreflex control of heart rate due to the sympatho-inhibition caused by the increase in NO production in the RVLM (7). However, it has not been determined whether the inhibition of oxidative stress in the RVLM improves the impaired baroreflex control of the heart rate of SHRSP or not.

The 3-hydroxy-3-methylglutaryl coenzyme A (HMG-CoA) reductase inhibitors (statins) are potent inhibitors of cholesterol biosynthesis, and statins have reported to have an anti-oxidant effect (8). Previously, we have demonstrated that orally atorvastatin increases the expression of NO synthase in the brain of SHRSPs (9), and that NO in the RVLM improves the impaired baroreflex control of heart rate in SHRSPs (7). These results suggested that orally atorvastatin might have the potential to improve the baroreflex control of heart rate in SHRSPs. Moreover, orally atorvastatin also inhibited the sympathetic nerve activity through the decrease in oxidative stress in the RVLM of SHRSPs (10).

Therefore, the aim of the present study was to investigate the effect of oral-administered atorvastatin on the baroreflex control of heart rate through its anti-oxidative stress in the RVLM of SHRSPs.

Materials and Methods

Animals and General Procedures

Twelve-week-old male SHRSPs/Izm and Wistar-Kyoto (WKY) rats (280 to 340g; SLC Japan, Hamamatsu, Japan) were fed a standard rodent diet. Food and tap water were available *ad libitum* throughout the study. The rats were kept in a room maintained at a constant temperature and humidity under a 12-h light period between 8:00 AM and 8:00 PM. After adaptation to these conditions over at least 2 weeks, SHRSPs were divided into two groups: 1) atorvastatin-treated SHRSP, treated with atorvastatin of 20mg/kg/day for 28 days, and 2) control-SHRSPs, treated with vehicle (0.5% methyl cellulose). All drugs were dissolved in 0.5% methyl cellulose and administered by gastric gavage everyday. Systolic blood pressure (SBP) and heart rate were measured using the tail-cuff method (BP-98A; Softron, Tokyo, Japan). We calculated the urinary norepinephrine excretion for 24 h as an indicator of sympathetic nerve activity, as described previously (4–7,10). To obtain the RVLM tissues, the rats were deeply anesthetized with sodium pentobarbital (100 mg/kg IP) and perfused transcardially with phosphate buffer saline (PBS) (150 mol/L NaCl, 3 mmol/L KCl, and 5 nmol/L phosphate; pH 7.4, 4°C). The brains were removed quickly, and sections 1 mm thick were obtained with a cryostat at -7 ± 1°C. The RVLM was defined according to a rat brain atlas as described previously (4–7,10), and obtained by a punch-out technique. This study was reviewed and approved by the committee on ethics of Animal Experiments, Kyushu University Graduate School of Medical Sciences, and conducted according to the Guidelines for Animal Experiments of Kyushu University.

Measurement of TBARS

The RVLM tissues were homogenized in 1.15% KCl (pH 7.4) and 0.4% sodium dodecyl sulfate, 7.5% acetic acid adjusted to pH 3.5 with NaOH. Thiobarbituric acid (0.3%) was added to the homogenate. The mixture was maintained at 5°C for 60 minutes, followed by heating to 100°C for 60 minutes. After cooling, the mixture was extracted with distilled water and *n*-butanolpyridine (15:1) and centrifuged at 1600 *g* for 10 minutes. The absorbance of the organic phase was measured at 532 nm. The amount of thiobarbituric acid-reactive substances (TBARS) was determined by absorbance, as described previously (4,10).

Measurement of Baroreflex Sensitivity by Spontaneous Sequence Method

Rats were initially anesthetized with sodium pentobarbital (50 mg/kg IP followed by 20 mg · kg^{-1} · h^{-1} IV). A catheter was inserted into the femoral artery to record arterial blood pressure, and a heart rate (HR) was derived from the blood pressure recording. The other catheter was also inserted into the femoral vein to allow for intravenous infusion of sodium pentobarbital. A tracheal cannula was connected to a ventilator, and the rats were artificially ventilated. Sequence analysis detected sequences of three or more beats in which there was an increase both in SBP and pulse interval (up sequence) or a decrease both in SBP and pulse interval (down sequence). Baroreflex sensitivity (BRS) was estimated as the mean slope of the up sequences (up BRS), the down sequences (down BRS), and also the mean slope of all sequences (sequence BRS) (11,12).

Statistical Analysis

All values are expressed as mean ± SEM. Comparisons between any two mean values were performed using Bonferroni's correction for multiple comparisons. ANOVA was used to compare the blood pressure, HR, baroreflex sensitivity, and TBARS level in atorvastatin- or control-SHRSP and WKY. Differences were considered to be statistically significant at a P value of < 0.05.

Results

BP, HR, and Urinary Norepinephrine Excretion

Systolic blood pressure was significantly higher in atorvastatin-SHRSP and control-SHRSP than in WKY, and atorvastatin did not alter SBP in SHRSP (Figure 1A). Heart rate was significantly higher in atorvastatin-SHRSP and control-SHRSP than in WKY, and atorvastatin also did not alter HR in SHRSP (Figure 1B). Urinary norepinephrine excretion was significantly higher in atorvastatin- and control-SHRSP than in WKY, and was not different between control- and atorvastatin-SHRSP (Figure 2).

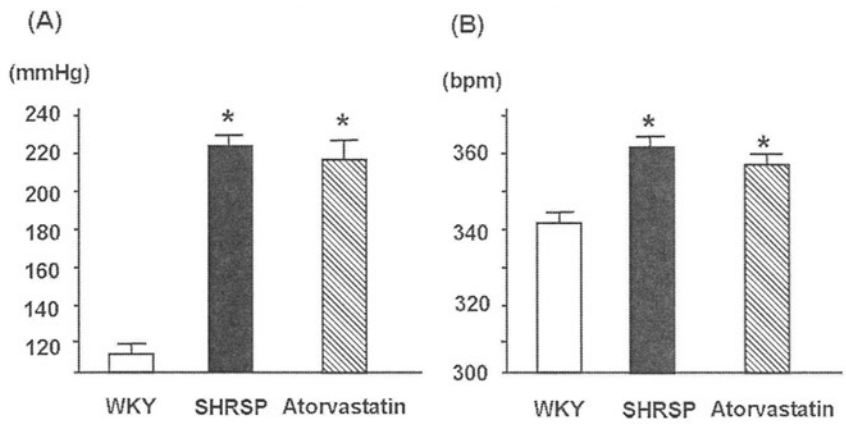

Figure 1. (A) Effects of the treatment with atorvastatin for 28 days on systolic blood pressure (SBP) of SHRSP and WKY. Data are shown as mean ± SEM (n = 5 for each group). *P < 0.05 vs. WKY. (B) Effects of the treatment with atorvastatin for 28 days on heart rate of SHRSP and WKY. Data are shown as mean ± SEM (n = 5 for each group). *P < 0.05 vs. WKY.

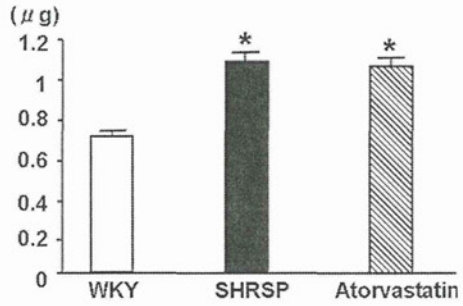

Figure 2. Effects of the treatment with atorvastatin for 28 days on 24-h urinary norepinephrine excretion of SHRSP and WKY. Data are shown as mean ± SEM (n = 5 for each group). *P < 0.05 vs. WKY.

TBARS Levels in the RVLM Tissues

Thiobarbituric acid-reactive substance levels in the RVLM were significantly higher in control- and atorvastatin-SHRSP than in WKY, and those of atorvastatin-SHRSP were significantly lower than those of control-SHRSP (0.70 ± 0.05 μmol/g wet wt vs. 0.91 ± 0.06 μmol/g wet wt, n = 5 for each, $P < 0.05$; Figure 3).

Baroreflex Sensitivity

Baroreflex sensitivity of control-SHRSP was significantly lower than that of WKY (9.2 ± 0.7 ms/mmHg vs. 19.1 ± 0.5 ms/mmHg, n = 5 for each, $P < 0.01$), and that of atorvastatin-SHRSP was significantly higher than that of control-SHRSP (14.8 ± 0.7 ms/mmHg vs. 9.2 ± 0.7 ms/mmHg, n = 5 for each, $P < 0.01$) (Figure 4).

Discussion

In the present study, we demonstrated for the first time that oral administration of atorvastatin improved the impaired baroreflex control of HR in SHRSP, and the improvement

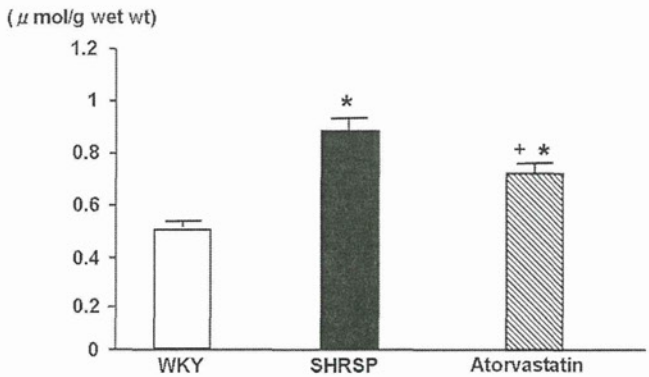

Figure 3. Effects of the treatment with atorvastatin for 28 days on TBARS levels in the RVLM of SHRSP and WKY. Data are shown as mean ± SEM (n = 5 for each group). *P < 0.05 vs. WKY; $^{+}$P < 0.05 vs. control-SHRSP.

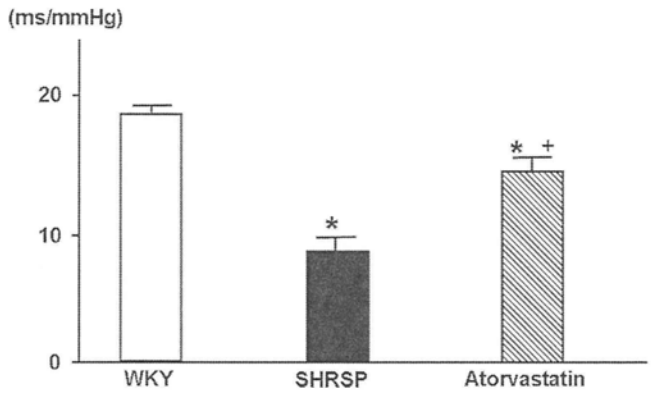

Figure 4. Effects of the treatment with atorvastatin for 28 days on baroreflex control of heart rate of SHRSP and WKY. Data are shown as mean ± SEM (n = 5 for each group). *P < 0.05 vs. WKY; $^{+}$P < 0.05 vs. control-SHRSP.

might be due in part to the inhibition of oxidative stress in the RVLM. Moreover, the improvement of baroreflex control of HR was independent of sympathetic nerve activity or blood pressure. We consider that these effects of atorvastatin benefit the treatment of the cardiovascular diseases with the disorder of baroreflex control.

In the present study, we demonstrated that atorvastatin improved the impaired baroreflex control without the reduction of BP or sympathetic nerve activity. Previously we reported that high-dose orally atorvastatin decreased BP and sympathetic nerve activity through the inhibition of oxidative stress in the RVLM (10). However, in the present study, low-dose atorvastatin did not decrease BP or sympathetic nerve activity, whereas oxidative stress in the RVLM was inhibited. We consider that this discrepancy is due to the smaller reduction of oxidative stress in the RVLM measure by TBARS compared to our previous study (10). We selected the lower dose of atorvastatin, because the effect of atorvastatin on baroreflex control should be examined in the condition excluded by BP and sympathetic nerve activity lowering effects. Moreover, baroreflex control is one of the key mechanisms responsible for the short-term control of BP. Impairment of this reflex has been found in a number of conditions, such as aging (13), heart failure (14), post-myocardial infarction (15), and the impairment of baroreflex sensitivity is known as the predictive factor of mortality in the hypertension (16). From the results in the present study, we consider that atorvastatin benefits the treatment for cardiovascular diseases.

The mechanisms in which atorvastatin improved the baroreflex control have not been determined in the present study. We consider that one of the possibilities in the mechanisms was the inhibition of oxidative stress in the RVLM, because the oxidative stress is the important modulator on the sympathetic nerve activity (4,10). Moreover, NO in the RVLM of SHRSPs improved the baroreflex control of HR (7). The inhibition of oxidative stress due to atorvastatin will contribute to the increase in NO in the RVLM of SHRSP and to the improvement of baroreflex control of HR.

A recent study suggests that the reduction of BP by clinical doses of statin is small but significant (17). However, the change in BP in the previous clinical study is significantly smaller than that in the present and previous animal study (10). Moreover, we are not able to determine the oxidative stress in the brain of human *in vivo* now and to determine whether the clinical doses of atorvastatin have the anti-oxidant effect in the

brain of the hypertensive patients. However, in the present study, oxidative stress in the RVLM is significantly reduced and baroreflex sensitivity is significantly improved by atorvastatin, whereas BP and sympathetic nerve activity are not altered. These results suggest that oxidative stress is inhibited and baroreflex sensitivity is improved by atorvastatin whose dose is insufficient for the reduction of blood pressure or sympathetic nerve activity. The improvement of baroreflex sensitivity could not be explained by the effect of atorvastatin on peripheral mechanisms, and we consider that baroreflex sensitivity is improved by the central action of atorvastatin. Clinical studies suggest that clinical doses of statins have the beneficial effect on arrhythmic sudden death and ventricular arrhythmia in the patients with heart failure, and these effects may be due to the improvement of the imbalance between sympathetic and parasympathetic nerve activity (18). It is necessary to examine the effect of clinical doses of atorvastatin on baroreflex sensitivity in a clinical study.

There are some limitations in the present study. First, we measured TBARS levels as the parameter of oxidative stress in the brain. Thiobarbituric acid-reactive substance levels are an indirect marker of oxidative stress, and there are other methods to measure oxidative stress. However, we previously measured oxidative stress directly in the brain of SHRSP and WKY using electron spin resonance spectroscopy and confirmed that TBARS levels are comparable to the levels of oxidative stress measured by electron spin resonance spectroscopy in the brain (4). The results suggest that TBARS levels are a valid parameter of oxidative stress in the brain. Second, we did not examine the TBARS levels in other areas of the brain, such as caudal ventrolateral medulla, nucleus tractus solitarii, paraventricular nucleus, cortex, hypothalamus, and cerebellum. We consider that these effects of atorvastatin was not unique in the RVLM, and we did not exclude the possibility that atorvastatin influences those areas thereby improving baroreflex control of HR in the present study. However, RVLM is the vasomotor center, and the integrated various inputs from other regions to RVLM influence the sympathetic outflow (1–3). Although it would be interesting to examine these parameters in other regions of the brain, we targeted the changes of oxidative stress in the RVLM due to atorvastatin in the present study.

Conclusions

Our results suggest that oral administration of atorvastatin improved the baroreflex control of heart rate due to the inhibition of oxidative stress in the RVLM of SHRSP.

Acknowledgments

We are grateful to Pfizer. USA, for supplying atorvastatin. This study was supported by a Grant-in-Aid for Scientific Research from the Japan Society for the Promotion of Science (B19390231), and in part, by the Health and Labor Sciences Research Grant for Comprehensive Research in Aging and Health Labor and Welfare of Japan.

Declaration of Interest

The authors report no conflicts of interest. The authors alone are responsible for the content and writing of the paper.

References

1. Dampney RA. Functional organization of central pathways regulating the cardiovascular system. *Physiol Rev* 1994;74:323–364.
2. Miyawaki T, Goodchild AK, Pilowsky PM. Evidence for a tonic GABA-ergic inhibition of excitatory respiratory-related afferents to presympathetic neurons in the rostral ventrolateral medulla. *Brain Res* 2002;924:56–62.
3. Guyenet PG. The sympathetic control of blood pressure. *Nat Rev Neurosci* 2006;7:335–346.
4. Kishi T, Hirooka Y, Kimura Y, Ito K, Shimokawa H, Takeshita A. Increased reactive oxygen species in rostral ventrolateral medulla contribute to neural mechanisms of hypertension in stroke-prone spontaneously hypertensive rats. *Circulation* 2004;109:3257–3262.
5. Kishi T, Hirooka Y, Sakai K, Shigematsu H, Shimokawa H, Takeshita A. Overexpression of eNOS in the RVLM causes hypotension and bradycardia via GABA release. *Hypertension* 2001;38:896–901.
6. Kishi T, Hirooka Y, Ito K, Sakai K, Shimokawa H, Takeshita A. Cardivascular effects of overexpression of endothelial nitric oxide synthase in the rostral ventrolateral medulla in stroke-prone spontaneously hypertensive rats. *Hypertension* 2002;39:264–268.
7. Kishi T, Hirooka Y, Kimura Y, Sakai K, Ito K, Shimokawa H, Takeshita A. Overexpression of eNOS in RVLM improves impaired baroreflex control of heart rate in SHRSP. *Hypertension* 2003;41:255–260.
8. Laufs U, La Fata V, Plutzky J, Liao JK. Upregulation of endothelial nitric oxide synthase by HMG-CoA reductase inhibitors. *Circulation* 1998; 97:1129–1135.
9. Kishi T, Hirooka Y, Mukai Y, Shimokawa H, Takeshita H. Atorvastatin causes depressor and sympatho-inhibitory effects with upregulation of nitric oxide synthase in stroke-prone spontaneously hypertensive rats. *J Hypertens* 2003;21:379–386.
10. Kishi T, Hirooka Y, Shimokawa H, Takeshita A, Sunagawa K. Atorvastatin reduces oxidative stress in the rostral ventrolateral medulla in stroke-prone spontaneously hypertensive rats. *Clin Exp Hypertens* 2008;30:1–9.
11. Waki H, Kasparov S, Wong LF, Murphy D, Shimizu T, Paton JFR. Chronic inhibition of eNOS activity in nucleus tractus solitarii enhances baroreceptor reflex in conscious rats. *J Physiol* 2003;546:233–242.
12. Waki H, Katahira K, Polson JW, Kasparov S, Murphy D, Paton JFR. Automation of analysis of cardiovascular autonomic function from chronic measurements of arterial pressure in conscious rats. *Exp Physiol* 2006;91:201–213.
13. Latinen T, Hartikainen J, Vanninen E, Niskanen L, Geelen G, Lansimies E. Age and gender dependency of baroreflex sensitivity in healthy subjects. *J Appl Physiol* 1998;84:576–583.
14. Mortara A, La Rovere MT, Pinna GD, Prpa A, Maestri R, Fedo O, Pozzoli M, Opasich C, Tavazzi L. Arterial baroreflex modulation of heart rate in chronic heart failure: Clinical and hemodynamic correlates and prognostic implications. *Circulation* 1997;96:3450–3458.
15. Farrell TG, Odemuyiwa O, Bashir Y, Gripps TR, Malik M, Ward DE, Camm AJ. Prognostic value of baroreflex sensitivity testing after acute myocardial infarction. *Br Heart J* 1992; 67:129–137.
16. Hesse C, Charkoudian N, Liu Z, Joyner MJ, Eisenach JH. Baroreflex sensitivity inversely correlates with ambulatory blood pressure in healthy normotensive humans. *Hypertension* 2007;50:41–46.
17. Golomb BA, Dimsdale JE, White HL, Ritchie JB, Criqui MH. Reduction in blood pressure with statins: Results from the USCD Statin Study, a randomized trial. *Arch Intern Med* 2008;168:721–727.
18. Goldberger JJ, Subacius H, Schaechter A, Howard A, Berger R, Shalaby A, Levine J, Kadish AH: DEFINITE Investigators. Effects of statin therapy on arrhythmic events and survival in patients with nonischemic dilated cardiomyopathy. *J Am Coll Cardiol* 2006;48:1228–1233.